The Astrophysical Journal, 646:420–428, 2006 July 20

M33 X-7: ChASeM33 REVEALS THE FIRST ECLIPSING BLACK HOLE X-RAY BINARY

W. Pietsch and F. Haberl
Max-Planck-Institut für extraterrestrische Physik, Giessenbachstrasse, 85741 Garching, Germany; wnp@mpe.mpg.de

M. Sasaki, T. J. Gaetz, and P. P. Plucinsky
Harvard-Smithsonian Center for Astrophysics, 60 Garden Street, Cambridge, MA 02138

P. Ghavamian
Department of Physics and Astronomy, Johns Hopkins University, 3400 North Charles Street, Baltimore, MD 21218-2686

K. S. Long
Space Telescope Science Institute, 3700 San Martin Drive, Baltimore, MD 21218

and

T. G. Pannuti
Spitzer Science Center, Jet Propulsion Laboratory/California Institute of Technology, Mail Stop 220-6, Pasadena, CA 91125
Received 2005 December 29; accepted 2006 March 24

ABSTRACT

The first observations conducted as part of the *Chandra* ACIS survey of M33 (ChASeM33) sampled the eclipsing X-ray binary M33 X-7 over a large part of the 3.45 day orbital period and have resolved eclipse ingress and egress for the first time. The occurrence of the X-ray eclipse allows us to determine an improved ephemeris of mid-eclipse and binary period as HJD $(2,453,639.119 \pm 0.005) \pm N(3.453014 \pm 0.000020)$ and constrain the eclipse half-angle to $26\overset{\circ}{.}5 \pm 1\overset{\circ}{.}1$. There are indications for a shortening of the orbital period. The X-ray spectrum is best described by a disk blackbody spectrum typical for black hole X-ray binaries in the Galaxy. We find a flat power density spectrum, and no significant regular pulsations were found in the frequency range of 10^{-4} to 0.15 Hz. *HST* WFPC2 images resolve the optical counterpart, which can be identified as an O6 III star with the help of extinction and color corrections derived from the X-ray absorption. Based on the optical light curve, the mass of the compact object in the system most likely exceeds $9\,M_{\odot}$. This mass, the shape of the X-ray spectrum, and the short-term X-ray time variability identify M33 X-7 as the first eclipsing black hole high-mass X-ray binary.

Subject headings: binaries: eclipsing — galaxies: individual (M33) — X-rays: binaries — X-rays: individual (M33 X-7)

Online material: color figures

1. INTRODUCTION

M33 X-7 (hereafter X-7) was detected as a variable source by the *Einstein* observatory with a maximum luminosity in the 0.15–4.5 keV band (assuming an absorption column of 10^{21} cm^{-2}) that exceeds 10^{38} ergs s^{-1} (Long et al. 1981; Markert & Rallis 1983). The source stayed active in all subsequent observations. Its variability was explained by an eclipsing X-ray binary (XRB) with an orbital period of 1.7 days and an eclipse duration of ~0.4 days (Peres et al. 1989; Schulman et al. 1993, 1994). Based on *Röntgensatellit* (*ROSAT*) and *Advanced Satellite for Cosmology and Astrophysics* (*ASCA*) data (Larson & Schulman 1997; Dubus et al. 1999, hereafter DCL99), the orbital period was found to be twice as long. DCL99 described the shape of the eclipse by a slow ingress ($\Delta\Phi_{\rm ingress} = 0.10 \pm 0.05$), an eclipse duration of $\Delta\Phi_{\rm eclipse} = 0.20 \pm 0.03$, and a fast eclipse egress ($\Delta\Phi_{\rm egress} = 0.01 \pm 0.01$) with an ephemeris for the mid-eclipse time of HJD $2,448,631.5 \pm 0.1 + N(3.4535 \pm 0.0005)$. DCL99 also reported 3 σ evidence for a 0.31 s pulse period. They came to that conclusion by splitting Position Sensitive Proportional Counter (PSPC) and High Resolution Imager (HRI) data of 500 s intervals of continuous data where X-7 was positively detected and calculating the summed Rayleigh power spectrum. The linearly binned power spectrum showed a significant excess (at 99.9% confidence) at the proposed period when compared to simulated data assuming a Poisson distribution with the X-7 mean flux. The signal is broader than what would be expected from a simple sinusoidal pulse. It was not possible to check if the variability is coherent. DCL99 conclude, "Although pulsed emission seems a reasonable assumption, the power excess could arise from variability of a different nature (e.g., broadband variability increasing the chance of spurious detection)." The orbital period, pulse period, and observed X-ray luminosity are remarkably similar to those of the Small Magellanic Cloud neutron star XRB SMC X-1 (Liu et al. 2000). X-7 was the first and only identified eclipsing accreting binary system with an X-ray source in an external galaxy other than the Magellanic Clouds before the detection of similar behavior based on *XMM-Newton* and *Chandra* data of the NGC 253 X-ray source RX J004717.4−251811 (Pietsch et al. 2003).

Pietsch et al. (2004, hereafter PMM04) analyzed several observations of the *XMM-Newton* M33 survey and an archival *Chandra* observation in which X-7 was in the field of view. The observations cover a large part of the 3.45 day orbital period, but not eclipse ingress and egress. PMM04 detected emission of X-7 during eclipse as well as a soft X-ray spectrum of the source out of eclipse that can best be described by bremsstrahlung or disk blackbody models. No significant regular pulsations of the source in the range 0.25–1000 s were found. The average source luminosity out of eclipse was 5×10^{37} ergs s^{-1} (0.5–4.5 keV, corrected for Galactic foreground absorption). In a special analysis of

TABLE 1
Chandra Observations of the ChASeM33 Program Covering M33 X-7

ChASeM33 Field (1)	ObsID (2)	Observation Dates[a] (3)	Elapsed Time (ks) (4)	ACIS CCD-ID (5)	Off Axis (arcmin) (6)	X-7 Binary	
						Phase[b] (7)	Cycle[b] (8)
2.....	6378	2005 Sep 21	112	7	17.9	0.675–1.044	−2, −1
5.....	7170	2005 Sep 26	41	1	1.6	0.200–0.334	0
	7171	2005 Sep 29	38	1	1.6	0.041–0.165	1
	6384	2005 Oct 1	22	1	1.6	0.832–0.905	1
6.....	6386	2005 Oct 31	15	0	7.2	0.365–0.412	10
	7196	2005 Nov 2	23	0	7.2	0.928–1.002	10, 11
	7197	2005 Nov 3	13	0	7.2	0.144–0.185	11
	7198	2005 Nov 5	22	0	7.2	0.798–0.868	11
	7199	2005 Nov 6	15	0	7.2	0.017–0.063	12
	7208	2005 Nov 21	12	1	7.3	0.622–0.660	16
4.....	6382	2005 Nov 23	73	2	9.7	0.071–0.312	17
	7226	2005 Nov 26	25	2	9.7	0.841–0.925	17

[a] Date of start of observation.
[b] With respect to eclipse center HJD 2,453,639.119 and orbital period 3.453014 days (see text).

DIRECT[1] observations, PMM04 identified as the optical counterpart a B0 I to O7 I star of 18.89 mag in V that shows the ellipsoidal light curve of a high-mass X-ray binary (HMXB) with the X-7 binary period. Based on the location of the X-ray eclipse and the optical minima, PMM04 derived an improved binary ephemeris and argued that the compact object in the system is a black hole. Those authors reached this conclusion based on the mass of the compact object derived from orbital parameters and the optical companion mass, the lack of pulsations, and the X-ray spectrum. X-7 would be the first detected eclipsing high-mass black hole XRB.

ChASeM33 is a very large program that will accumulate in seven deep pointings, each 200 ks in length, a total exposure of 1.4 Ms. During several of these pointings X-7 is in the field of view. We report here on ChASeM33 observations of X-7 spread over just 20 binary orbits, which resolved for the first time the eclipse ingress and egress and allowed us to constrain the light curve of X-7 for binary phases around eclipse. Preliminary results of the first observations were announced by Sasaki et al. (2005). In addition, we identify the source on archival *Hubble Space Telescope* (*HST*) Wide Field Planetary Camera 2 (WFPC2) images. Throughout the paper, we assume a distance to M33 of 795 kpc (van den Bergh 1991).

2. *CHANDRA* OBSERVATIONS AND RESULTS

X-7 was sampled by the ACIS-S3 chip in one *Chandra* observation and by the I0, I1, and I2 chips during 11 additional observations. Table 1 summarizes these observations, giving observation identification (ObsID) in column (1), observation start date (col. [2]), elapsed time (col. [3]), the ACIS chip covering X-7 (col. [4]), the offset of X-7 from the pointing direction (col. [5]), and the X-7 binary phase during the observation (col. [6]) using ephemeris that is discussed in §§ 2.1 and 4.1. The source brightness varied from $\sim 3 \times 10^{-3}$ counts s^{-1} to $\sim$0.2 counts s^{-1}, normalized to ACIS-I on axis.

Of the pointings considered here, the field 5 position of X-7 is located close enough to the optical axis to result in significant pile-up, particularly during the high phase. To correct the light curve for the effects of pile-up, we used the best-fit model for unpiled data from the other pointings (see § 2.2) and applied a pile-up (phabs/diskbb) model within XSPEC. We estimated the pile-up parameters by fitting simultaneously the high-state data for ObsID 6382 (insignificant pile-up) and ObsIDs 7170 and 7171 (significant pile-up). The phabs and diskbb models were set to their best-fit values from the unpiled spectra; the diskbb normalizations were tied for all three data sets. All of the pile-up model parameters except the grade-morphing parameter α were frozen. For a description of the pile-up model, see Davis (2001). The pile-up parameters were set to their default values, but the fr_time parameter was frozen at 3.2 for ObsIDs 7070 and 7071, and at 0 for ObsID 6382; this has the effect of turning off the pile-up model component for ObsID 6382. The resulting reduced χ^2 of the fit was 0.97, and the corresponding value for α was $0.692^{+0.114}_{-0.116}$ (90% confidence limits). Using the fitted value for α, a correction curve was generated by evaluating the ratio of the XSPEC "model-predicted rate" without pile-up (fr_time=0) to the corresponding rate with pile-up (fr_time=3.2), as a function of the model-predicted rate (with pile-up). This ratio was used to correct the observed count rates of ObsIDs 6384, 7070, and 7071 for the effects of pile-up.

For the spectral analysis we used standard level 2 event files cleaned for columns with higher background rates than adjacent columns. In the observations of fields 4 and 5, counts from X-7 are rejected when the source is moving across rejected columns (due to the satellite dithering). This effect creates spurious periods in period analysis and can reduce the counts in 1000 s integration intervals by varying amounts (up to more than 30%). Therefore, we created new level 2 event files for broadband time variability analysis that did not reject these columns. We correct for the detection efficiency at different off-axis angles, using factors derived from response files for the different CCDs and off-axis positions assuming the disk blackbody spectrum derived in § 2.2. We normalized the count rates to a CCD 3 on-axis rate.

The data analysis was performed using tools in the ESO-MIDAS version 05SEPpl1.0, EXSAS version 03OCT_EXP, CIAO version 3.2, and LHEASOFT version 5.3 software packages, as well as the imaging application DS9 version 3.0b6.

2.1. *Time Variability*

During ObsIDs 6378 and 7171 we observed transitions by X-7 into and out of eclipse, respectively. We sampled both background

[1] For information on the DIRECT project, see http://cfa-www.harvard.edu/~kstanek/DIRECT/.

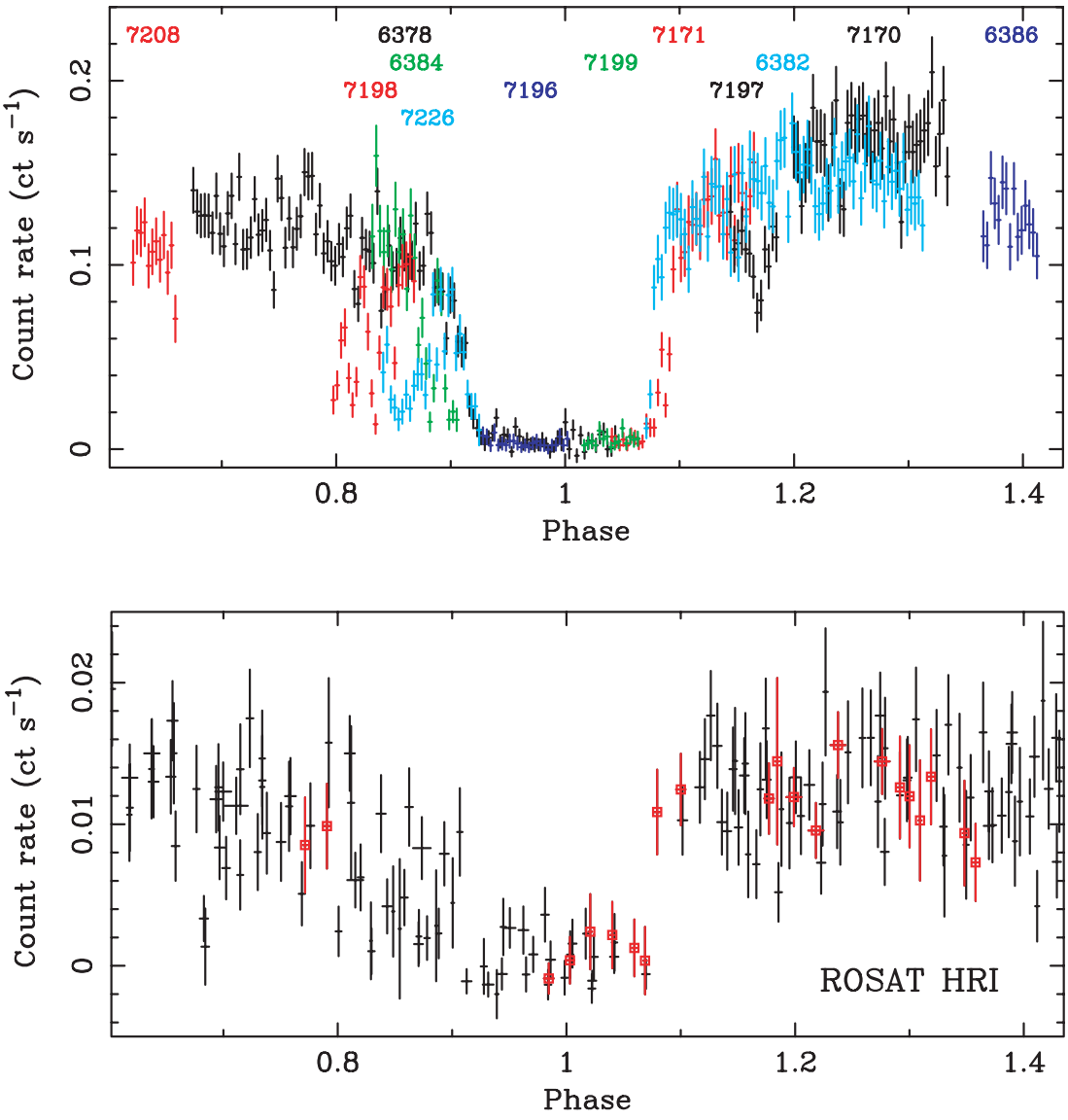

FIG. 1.—Light curve of the X-ray binary X-7. *Top*: *Chandra* ACIS light curve in the 0.5–5.0 keV band. Individual observations are marked by their ObsID. *Bottom*: *ROSAT* HRI light curve (0.1–2.4 keV). Observations around eclipse on JD 2,449,571 are marked as red squares.

and solar system barycenter-corrected light curves of X-7 with a time resolution of 1000 s. To increase the signal-to-noise ratio (S/N) specifically in the far off-axis ObsID 6378, we restricted the analysis to the 0.5–5 keV band, which covers most of the source flux. Further subdividing this energy band into a hard and soft band did not show any significant hardness ratio changes of the ingress and egress behavior, as could be expected based on *European X-Ray Observatory Satellite* (*EXOSAT*) observations of LMC X-4 and Her X-1 (see Figs. 78 and 79 in Dennerl 1991). To determine eclipse start and end times, we approximated the light curves assuming constant count rates within and out of eclipse, and a linear transition in between, using a χ^2 minimization technique. We searched for 1 σ errors of the eclipse start and end times, respectively, assuming those to be the only interesting parameter for the fit.

In ObsID 6378, the transition into eclipse lasted 12.75 ks and ended at HJD $2,453,635.4110 \pm 0.0037$. The transition out of eclipse in ObsID 7171 started at HJD $2,453,642.8272 \pm 0.0052$ and lasted for 10.52 ks. From these ingress and egress times separated by two orbital periods, we directly derive the mid-eclipse ephemeris of the eclipse in between to HJD $2,453,639.119 \pm 0.005$. Assuming this epoch as phase zero and a binary period of 3.453014 days (see § 4.1), we calculated light curves of all X-7 observations (Fig. 1). We also determine an eclipse duration of less than 0.147 ± 0.006 in phase, corresponding to an eclipse half-angle of $26\overset{\circ}{.}5 \pm 1\overset{\circ}{.}1$.

ObsIDs 7196 and 7199 fully fall into eclipse. ObsID 6384 at phase 0.83–0.90 indicates a much longer transition into eclipse than ObsID 6378. ObsID 7198 shows dipping behavior well before eclipse, with a return to the out-of-eclipse intensity level at the end. ObsID 6382 shows a second egress from eclipse that is significantly faster than the one 16 orbits earlier (ObsID 7171). However, the observation starts during egress, and the phase range within eclipse is not covered. ObsID 7226 covers eclipse ingress at the end of the same orbit and again shows strong dipping well before the ingress. Eclipse egress and ingress times are consistent with the times derived above. Generally speaking, the variability of X-7 before eclipse (phase 0.7–0.9) seems to be much more pronounced in individual observations than after eclipse (phase 1.1–1.4). Average count rates in eclipse and out of eclipse are 0.003 and 0.15 counts s^{-1}, respectively. This out-of-eclipse count rate varies in different binary orbits by factors of 1.3, and there are

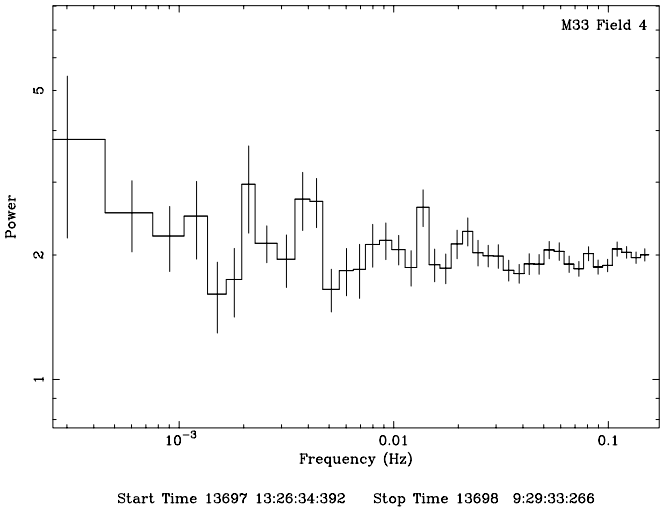

FIG. 2.—*Chandra* ACIS power density spectrum of X-7 from ObsID 6382, using 23 intervals of 1024 3.241 s bins.

residual short-term fluctuations that can be described by dips with a similar amplitude and a duration of several 1000 s, also outside the pre-eclipse phase.

To search for pulsations, we extracted light curves in the 0.5–5 keV band from the longest observations after eclipse, ObsIDs 6382 and 7170. We created power density spectra in the frequency range of 10^{-4} to 0.15 Hz and found no significant periodic signal with a 3 σ upper limit of 5.3% for sinusoidal variations. A power density spectrum derived from ObsID 6382 by adding the power spectra from 23 intervals of 3319 s length (1024 time bins with the instrument resolution of 3.241 s) is shown in Figure 2. The power spectrum is flat at a value of 2.

2.2. *Energy Spectra*

We analyzed energy spectra of X-7 for all observations. For ObsIDs 6378 and 7171, times out of eclipse, during ingress and egress, and in eclipse were handled separately. Absorbed power-law, bremsstrahlung, and disk blackbody models (which were found to best represent the *XMM-Newton* and *Chandra* spectra analyzed by PMM04) were first fit to the individual spectra. The power-law fit to the spectrum obtained from ObsID 6382 (which has the highest statistical quality) yields an unacceptable fit with a reduced χ^2 of 1.92, while bremsstrahlung and disk blackbody models result in χ^2_r of 1.45 and 1.32, respectively. The derived parameters are consistent within the errors for all spectra, including the spectra accumulated during eclipse ingress and egress and during ObsID 7198 when the source shows high variability. Therefore, we performed a simultaneous fit with the disk blackbody model to the spectra of eight out-of-eclipse observations, excluding times when the X-ray source was in eclipse and forcing the absorbing column density to be the same for all observations (this reduces the number of free fit parameters compared to the individual fits). The resulting inner disk temperature was systematically higher (at $\sim$1.3 keV) for ObsIDs 6384, 7170, and 7171: these are the observations that include X-7 nearly on axis. The most likely reason for the "harder" spectra is pile-up, and we therefore excluded these three spectra from further analysis. The fit to the remaining five spectra from ObsIDs 6378, 6382, 6386, 7197, and 7198 shows no significant differences in the inner disk temperature, and therefore this parameter was also forced to be the same in the simultaneous fit. We refit the power-law and bremsstrahlung models for comparison. The best fit is obtained with the disk blackbody model yielding a χ^2_r of 1.10. The χ^2_r for the best-fit bremsstrahlung and power-law models are 1.16 and 1.44, respectively. The derived spectral parameters are similar to the ones reported by PMM04: disk blackbody with inner disk temperature $kT = 0.99 \pm 0.03$ keV and $N_{\rm H} = (0.95 \pm 0.10) \times 10^{21}$ cm^{-2}, bremsstrahlung with temperature $kT = 2.74 \pm 0.13$ keV and $N_{\rm H} = (2.05 \pm 0.12) \times 10^{21}$ cm^{-2}, and power-law with photon index $\gamma = 2.38 \pm 0.05$ and $N_{\rm H} = (3.32 \pm 0.17) \times 10^{21}$ cm^{-2}. The best-fit disk blackbody model is shown in Figure 3.

The normalization of the disk blackbody model is given by $K = (r_{\rm in}/d)^2(\cos i)$, with the inner disk radius $r_{\rm in}$ in km, the source distance d in units of 10 kpc, and the disk inclination i. The spectra show variations by a factor of $\sim$2 in normalization with $K = 0.054$ for ObsID 6378 and relative factors 0.58, 0.94, 1.13, and 1.37 for ObsIDs 7198, 7197, 6386, and 6382, respectively.

The $N_{\rm H}$ values for the models discussed above clearly indicate absorption within M33, or intrinsic to the source, in addition to the Galactic value (5.86×10^{20} and 6.37×10^{20} cm^{-2} in the direction of X-7, according to Dickey & Lockman [1990] and Stark et al. [1992], respectively). Absorbed and unabsorbed source fluxes in the 0.3–10 keV band are in the range $(5.4\text{–}12.6) \times 10^{-13}$ and $(6.2\text{–}14.7) \times 10^{-13}$ ergs cm^{-2} s^{-1}, respectively, based on the best-fit disk blackbody model. These fluxes correspond to source luminosities of $(4.1\text{–}9.6) \times 10^{37}$ and $(4.7\text{–}11.2) \times 10^{37}$ ergs s^{-1}, respectively.

The $N_{\rm H}$ value of the best-fit disk blackbody model indicates that X-7 lies on the near side of M33, as the absorbing column within M33 can be determined to $\sim 2.2 \times 10^{21}$ cm^{-2} from a $47'' \times 93''$ half-power beam width H I map (Newton 1980). From the $N_{\rm H}$ value we can compute the expected optical extinction $A_V = 0.53 \pm 0.06$ mag and $E(B - V) = 0.18 \pm 0.02$ using the standard relations (Predehl & Schmitt 1995). These numbers are in the range given by PMM04, who assumed that we see X-7 through less than half the absorbing column within M33.

2.3. *Improved Position*

X-7 was located in four of the five ChASeM33 fields observed so far. The source was closest to on axis (1.′58 off axis) in the field 5 observations (see Table 1). This results in the most compact point-spread function (PSF) and thus the most reliable position determination. To refine the absolute astrometry of the field 5 data, we searched the USNO-B1.0 and Two Micron All Sky Survey (2MASS) catalogs for close positional matches with X-ray sources. Similarly, to improve the statistics for X-ray centroiding, we worked with a merged data set for ObsIDs 6384, 7170, and 7171. We identified nine candidate optical/2MASS objects. Six were rejected because of far off-axis positions or a small number of counts. The remaining candidates were $\leq 7'$ off axis, except for one 2MASS object ($\sim$250 counts, 0.5–5 keV) that was 7.′8 off axis. We enhanced the number of candidates for registration by adding two isolated, centrally brightened supernova remnants (SNRs) with good radio positions (sources 57 and 64 from the list of Gordon et al. 1999) assuming that the finite size of SNRs, and potential differences in the X-ray versus radio distribution, do not bias the position determination. We determined the X-ray centroids based on an iterative σ-clipping algorithm applied to the 0.5–5 keV X-ray data. Based on an initial position estimate and clipping radius, the standard deviation of the radial distribution is evaluated, and points greater than a given number of standard deviations are rejected. The iteration of centroiding and rejecting events continues until the centroid converges to within a specified tolerance or for a fixed number of iterations (10). The difference in sky coordinates between the catalog position and the X-ray centroid position was evaluated for each source. The mean offset was

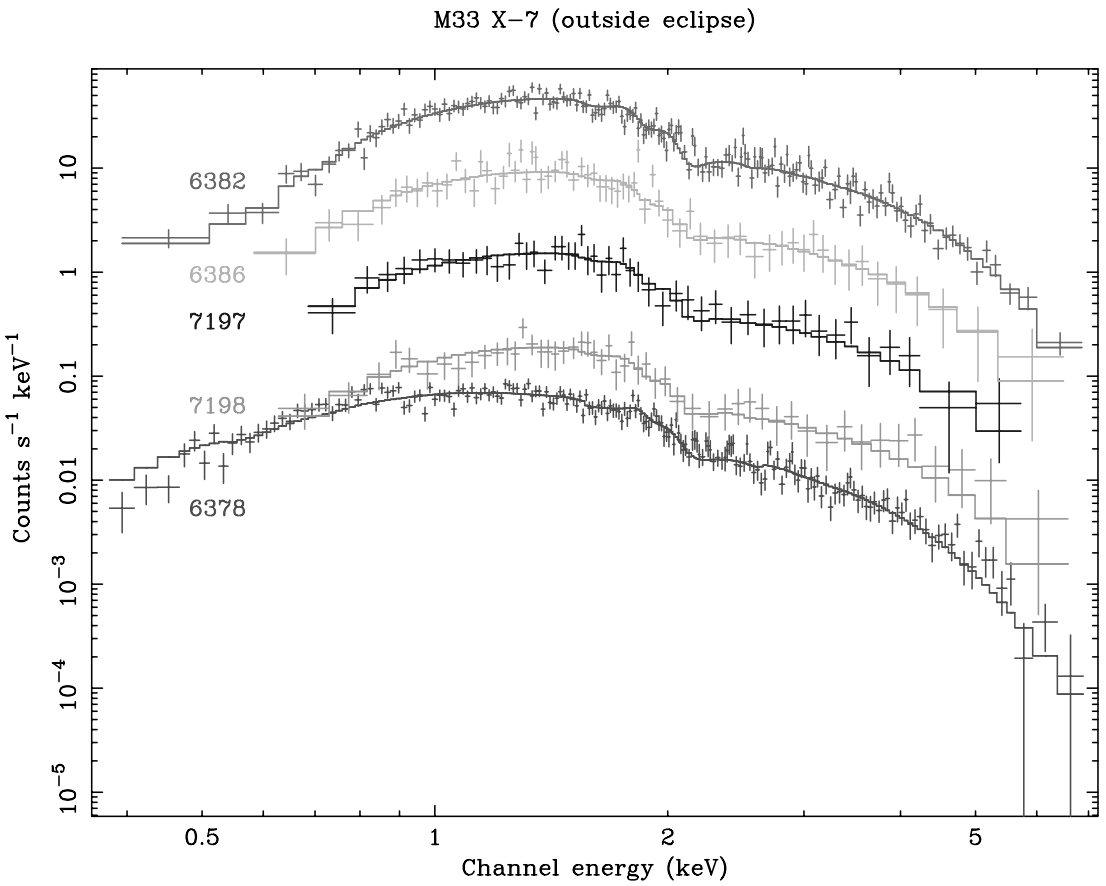

FIG. 3.—*Chandra* ACIS spectra of X-7 during high state. Data and the corresponding disk blackbody model are shown (see text). For a better representation, the spectra were multiplied successively by factors of 1, 5, 5^2, 5^3, and 5^4 from the bottom to the top. [*See the electronic edition of the Journal for a color version of this figure.*]

$\Delta x = (0\farcs23 \pm 0\farcs37)$, $\Delta y = (0\farcs32 \pm 0\farcs21)$. The centroid of the X-7 source was evaluated in the same way, and the resulting offset was applied to correct the sky position. Finally, the corresponding celestial coordinates were evaluated using the CIAO tool `dmcoords`; the aspect solution files (asol1 files) were used in order to correct the positions using the aspect offsets. The resulting X-7 position is R.A.(J2000.0) = $01^h33^m34\fs12$, decl.(J2000.0) = $+30^\circ32'11\farcs6$, with a combined error of $0\farcs5$. The position is within 2 σ of that given by PMM04 based on a registration using just one SNR.

3. OPTICAL OBSERVATIONS AND RESULTS

X-7 is located along the line of sight to the dense OB association HS 13 (Humphreys & Sandage 1980); it was identified by PMM04 with a specific star within this association, as a result of detection of regular (ellipsoidal) variations in *B* and *V* at the X-ray period. The OB association has been imaged with *HST* using WFPC2 in three filters: F336W, F439W, and F555W. The observing details are listed in Table 2. In an attempt to learn more about the optical counterpart to X-7, we retrieved relevant data sets from the MAST archive. Data retrieved from the archive are automatically reprocessed with the latest calibration files. After inspecting the individual exposures, we combined the two exposures taken with the F336W filter and the two taken in F439W (using the STSDAS task `gcombine`) to eliminate the effects of cosmic rays on the images.

TABLE 2
HST OBSERVATION LOG OF THE M33 X-7 FIELD

Data Set	Date	Time	Exposure (s)	Filter
u2tr0301t	1995 Oct 25	13:40:16	160	F555W
u2tr0302t	1995 Oct 25	13:45:17	400	F336W
u2tr0303t	1995 Oct 25	13:54:17	400	F336W
u2tr0304t	1995 Oct 25	14:04:17	500	F439W
u2tr0305t	1995 Oct 25	14:15:17	300	F439W

The position of the X-ray source as determined with *Chandra* is shown in Figure 5. Since the error in the astrometric solution of images in the *HST* pipeline is typically $\sim 1\farcs5$–$2''$, we attempted to reduce the positional uncertainty by registering the WFPC2 images to the USNO-B1.0 or 2MASS frames. Given the small field of view and greatly superior spatial resolution of the WFPC2 images, many sources identified in the USNO-B1.0 or 2MASS catalogs are resolved into multiple objects, making a unique match between stars in the image and sources in the catalog difficult. Therefore, we performed our astrometric corrections in two steps, taking advantage of the much larger field of view of the KPNO mosaic B image of M33 (Massey et al. 2001). First, we identified a sample of 25 isolated, bright USNO-B1.0 stars within $4\farcm5$ of X-7 to compute the shift required to bring the mosaic B image into the USNO-B1.0 frame. The rms positional error of these stars in the corrected mosaic image was unacceptably large ($0\farcs85$). We then tried the same procedure using 21 bright 2MASS stars located in isolated areas in the KPNO mosaic B image. The rms positional error of these stars in the corrected mosaic image was $0\farcs16$. We then used 10 bright, isolated stars in common between the mosaic B and F439W images (restraining the selection to the region covered by the WFPC2 CCD in which the X-7 counterpart was located) to compute the shift required. The rms

positional error in the shifted *HST* image was 0.″13. Combining the 0.″1 absolute uncertainty of the 2MASS position with the uncertainties listed above, the absolute astrometric uncertainty of the final registered F439W image is 0.″23.

We applied the calculated shifts above to the *HST* image. Figure 5 shows a $10'' \times 10''$ field from the F439W image centered on X-7. The black circle shows our best estimated position for the X-ray source from the *Chandra* image. The error circle of X-7 is 0.″5 in radius (see above). The *HST* positional accuracy is indicated by a plus sign. We also show the error quoted by PMM04 as a gray circle. The error circles overlap with a bright star, coincident with that proposed by PMM04 (based also on time variation arguments) as the donor star for the compact object.

We also carried out aperture photometry of the stars in the *HST* field (using the IRAF procedures `daofind` and `phot`). We find that the optical counterpart to X-7 with the WFPC2 resolution is not a blend of stars. PSF fits to the source in the F336W, F439W, and F555W images give FWHM compatible with the other pointlike sources in the images. The star about 0.″9 to the south, on the other hand, is just resolved in at least two equally bright sources that are separated by ∼0.″2. We can rule out the presence of another star of similar brightness at the position of the optical counterpart of X-7 to this distance, which corresponds to a projected separation at the distance of M33 of 0.8 pc.

The optical counterpart has apparent magnitudes of 17.6, 18.2, and 18.9 for the F336W, F439W, and F555W filters, respectively, in the STMAG system. The colors derived from these filters for the counterpart to X-7 are typical of the other bright stars ($m_V < 20.5$) in HS 13, as observed with WFPC2. The F336W, F439W, and F555W filters are centered approximately on the corresponding *U*, *B*, and *V* filters. Adopting a color transformation of 0.5 mag for *U*, 0.66 mag for *B*, and 0.03 mag for *V*, we find m_U of 18.1 mag, m_B of 18.8 mag, and m_V of 18.9 mag (i.e., $U - B$ of -0.7 mag, $B - V$ of -0.1 mag) for the optical counterpart to X-7.[2]

4. DISCUSSION

The well-sampled orbital light curve of X-7 indicates stronger variability before eclipse compared to after eclipse (Fig. 1). Variability at this phase is often observed in HMXBs and is explained by the viewing geometry through the innermost regions of the wind of the companion, and dense material following the compact object in its orbit (e.g., Haberl & Day 1992). Dense structures are created by the gravitational and radiative interactions of the compact object with the stellar wind (Blondin et al. 1990, 1991). This behavior is also reflected in the on-average longer eclipse ingress time and longer eclipse duration derived by DCL99.

Similarly to PMM04 we find residual emission from the source during eclipse. Residual emission during eclipse was measured from most eclipsing XRBs and can be explained by reprocessing of primary photons from the compact X-ray source in an extended accretion disk corona (which is not fully occulted) or by scattering in the companion atmosphere/stellar wind. Residual emission of up to ∼10% of the uneclipsed flux was reported (Haberl 1991; Lewis et al. 1992; Ebisawa et al. 1996), depending on system geometry and wind density. The X-7 residual emission of ∼4% is well within these limits.

4.1. *Improved Ephemeris*

DCL99 modeled the folded light curve from X-7 as a constant flux plus linear ingress and egress plus an eclipse interval with zero flux. It is obvious from their data (see their Fig. 1) that the eclipse egress is better determined than the eclipse center and duration. These strongly depend on the shape of the pre-eclipse dips contained in the light curve, as can be seen from the resolved pre-eclipse behavior in the *Chandra* data (Fig. 1). DCL99 did not determine the eclipse parameters from individual eclipses but only from the average light curve due to limited statistics. The time of eclipse egress is the best determined parameter. Unfortunately, in their paper they do not give this parameter separately, but only the center of eclipse and length of eclipse. In the following, we use eclipse egress times to determine an improved orbital period *P* and a possible period derivative $\dot{P}$.

Due to limited phase coverage, the *XMM-Newton* observations do not resolve eclipse ingress or egress. The time of eclipse egress can only be constrained to <0.02 in phase. Based on these data PMM04 restricted the time of eclipse egress to HJD $2,451,760.953 \pm 0.035$ (note the typographical error in egress time in PMM04, but the calculation used the number given here) and determined a time of mid-eclipse assuming the eclipse shape parameters of DCL99. With this mid-eclipse epoch and the one given by DCL99, PMM04 determined an improved orbital period.

The maximum eclipse duration of 0.147 ± 0.006 (§ 2.1) determined from individual observations is, as expected, significantly shorter than the one given by DCL99 (0.20 ± 0.03) from average orbit fitting. From the DCL99 ephemeris it is not possible to derive a well-defined eclipse egress time. The same is true for the *Einstein* results (Peres et al. 1989, hereafter PRC89). We therefore decided to reanalyze relevant *ROSAT* and *Einstein* data.

ROSAT PSPC observations of M33 were short compared to the HRI observations and did not cover the X-7 eclipse egress. We therefore restricted our reanalysis to *ROSAT* HRI data. After screening for high background, we combined data with continuous observation intervals that led to variable integration times of typically 1800 s (minimum 41 s, maximum 3791 s), depending on the duration of the scheduled observation and background. DCL99, in contrast, grouped the data in 3000 s averages. Only once is the eclipse egress closely monitored. In the *ROSAT* interval corresponding to ObsID 600488h, X-7 was still in eclipse, while in the following interval (corresponding to ObsID 600489h), less than 0.04 days later, X-7 already featured a count rate that indicated the source was out of eclipse. This allowed us to restrict the time of eclipse egress to HJD $2,449,571.724 \pm 0.018$. In another case, during ObsID 600020h-1, observations in eclipse and out of eclipse are separated by 0.26 days, which does not allow us to further constrain eclipse egress times.

PRC89 reported *Einstein* IPC and HRI observations of X-7. For the HRI observations PRC89 combined several continuous observation intervals to get significant data. For the IPC observations PRC89 simply integrated over individual continuous observations. Due to the better statistics in the IPC observations, we considered only IPC eclipse egress coverages (i.e., ObsID I2090; see also Fig. 1 of PRC89). In images of the observation, X-7 is only visible in the energy band 0.6–2.8 keV (PI 4–9). We therefore restricted the analysis to this energy band. We selected extraction position and area by comparison with the nearby bright central source X-8. We specifically investigated the "first rising episode at day 1.5" as identified by PRC89. In contrast to the report by PRC89, X-7 count rates during this period do not show increasing flux, but the source intensity is compatible with zero during all three intervals. In the next set of observation intervals, at around day 2, the source is clearly out of eclipse. This indicates an eclipse egress between HJD 2,444,087.840 and 2,444,088.255.

Combining the *ROSAT* eclipse egress boundaries with the *Chandra* ephemeris suggests an orbital period of 3.453014 ± 0.000020 days. The bottom panel of Figure 1 shows the *ROSAT*

[2] See http://www.stsci.edu/hst/stis/documents/handbooks/DataHandbookv4/.

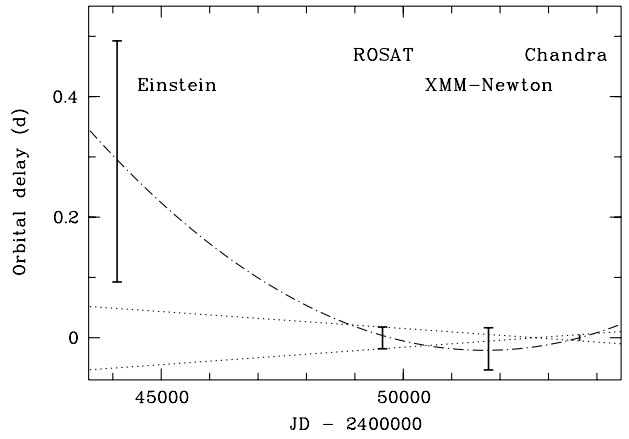

FIG. 4.—Deviation of eclipse egress times relative to the best orbital period of 3.453014 days and *Chandra* eclipse egress ephemeris. The dotted lines give the shortest and longest periods allowed by the *Chandra* and *ROSAT* data. The parabola assumes a period of 3.45294 days at the *Chandra* epoch, and orbital period decay rate of $\dot{P}_{\rm orb}/P_{\rm orb} = -4 \times 10^{-6}$ yr^{-1} (see text).

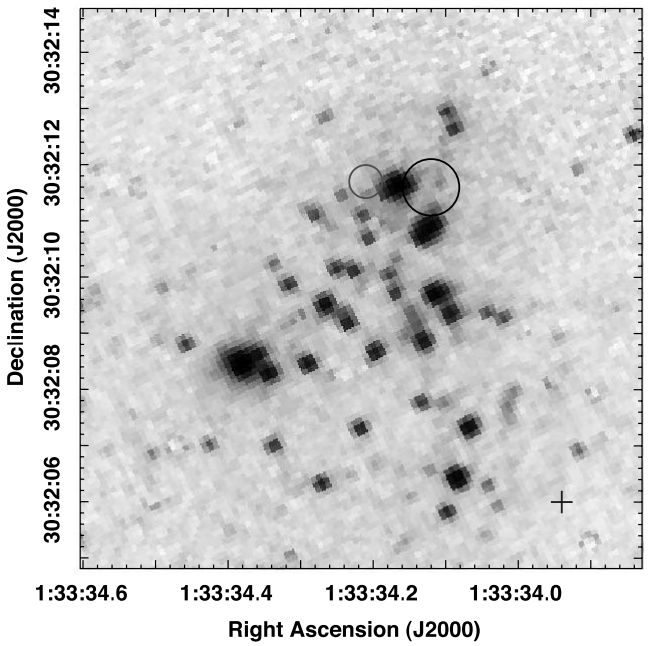

FIG. 5.—*HST* WFPC2 F439W $10'' \times 10''$ image of the HS 13 field with X-ray positions overlaid. The black circle gives *Chandra* position and error from field 5. The gray circle indicates the position given by PMM04 based on just one radio SNR. Image registration uncertainty is indicated by the plus sign in the lower right corner. [*See the electronic edition of the Journal for a color version of this figure.*]

HRI light curve folded with the above period and assuming the *Chandra* mid-eclipse epoch, for the same phase range as the *Chandra* data above. As can be seen in Figure 4, these ephemerides also are consistent with the boundaries determined for the *XMM-Newton* eclipse egress. However, they seem to miss the boundaries determined above for the *Einstein* IPC observation. If we assume a constant rate of change of the orbital period over this time, we can model all eclipse egresses. The parabola shown in Figure 4 assumes a period of 3.45294 days at the *Chandra* epoch and orbital period decay rate of $\dot{P}_{\rm orb}/P_{\rm orb} = -4 \times 10^{-6}$ yr^{-1}. It nicely models the average eclipse egress times of *XMM-Newton*, *ROSAT*, and *Einstein*. However, a small $\dot{P}_{\rm orb}/P_{\rm orb} = -0.7 \times 10^{-6}$ yr^{-1} and a period of 3.45302 days, or a much higher $\dot{P}_{\rm orb}/P_{\rm orb} = -7.5 \times 10^{-6}$ yr^{-1} and a period of 3.45285 days, would also still be consistent with all the eclipse egress boundaries.

The derived orbital decay for X-7 is well within the range of values determined for other HMXBs such as Cen X-3 [$(-1.738 \pm 0.004) \times 10^{-6}$ yr^{-1}; Nagase et al. 1992], SMC X-1 [$(-3.36 \pm 0.02) \times 10^{-6}$ yr^{-1}; Levine et al. 1993], or LMC X-4 [$(-9.8 \pm 0.7) \times 10^{-7}$ yr^{-1}; see, e.g., Safi Harb et al. 1996; Levine et al. 2000]. Such rapidly decreasing periods in HMXBs are most likely caused by tidal interaction between the compact object and its massive companion. As the orbit decays, the Roche lobe will descend into the companion's atmosphere, and mass transfer will increase to super-Eddington rates over a relatively short timescale. In the end, the compact object is expected to spiral into the envelope of the companion and in this way terminate the high-mass XRB phase of the evolution (see, e.g., Levine et al. 1993).

4.2. *The Optical Companion*

The *HST* WFPC2 images clearly resolve the dense OB association HS 13 (Humphreys & Sandage 1980). The optical counterpart is located to the north and is one of a pair of stars with similar luminosities: these stars are separated by $\sim 0''.9$. While the suggested counterpart is presumed to be a single source, the source to the south is a blend of at least two stars (elongation from south-southeast to north-northwest). The *HST* observations were carried out within 1 hour on 1995 October 25, corresponding to binary phase 0.76 using the ephemeris given in § 4.1. Phase 0.76 corresponds to the second maximum of the ellipsoidal light curve. Assuming the parameters of the optical light curve by PMM04 (sinusoidal fit with 0.033 mag amplitude), the correction to X-ray eclipse is +0.066 mag, resulting in corrected magnitudes m_B of 18.9 mag, and m_V of 19.0 mag for the optical counterpart to X-7. Magnitudes and colors are very close (within 0.1 mag) to values deduced by PMM04. X-7 is also included in the *UBVRI* photometry of stars in M31 and M33 from the survey of Local Group galaxies recently published by Massey et al. (2006). They give a position (registered with the USNO B1.0 frame) of R.A. (J2000.0) $= 01^{\rm h}33^{\rm m}34^{\rm s}.18$, decl.(J2000.0) $= +30^\circ 32' 11''.5$, about $0''.3$ east-southeast from the position in our registered *HST* image position (see Fig. 5). Their X-7 magnitude and colors ($m_V = 19.087 \pm 0.007$ mag, $m_{(B-V)} = -0.084 \pm 0.10$ mag, $m_{(U-B)} = -1.057 \pm 0.11$ mag) coincide with those determined by us within 0.2 mag. Part of the discrepancy may be due to the sampling at different binary phases.

The type and luminosity class of the star can be deduced from the absolute optical magnitude and color during eclipse when we see the optical surface that is mostly undisturbed by gravitational effects, an expected accretion disk, and heating by the X-ray source. To derive the absolute magnitude, the measured brightness has to be corrected for the distance (−25.50 mag for the assumed distance of 795 kpc) and for interstellar extinction, and the color has to be corrected for reddening. These corrections have been estimated from the absorption of the X-ray spectrum in § 2.2. Based on the *HST* values, the companion star should have an absolute M_V of −6.1 mag and $(B - V)_0$ of −0.3 mag. This corresponds to a giant star of spectral type O6 III that has a temperature of 39,500 K, a radius of 17 $R_\odot$, and a mass well above 20 $M_\odot$ (see Appendix E in Carroll & Ostlie 1996).

4.3. *M33 X-7: An Eclipsing Black Hole HMXB*

With the new eclipse duration and the better determination of the companion type on the basis of the extinction combined with the color excess corrections derived from the absorbing column of the X-ray spectrum of X-7, we can significantly improve the

TABLE 3
M33 X-7 Binary Parameters for Different Inclinations Determined with PHOEBE

Inclination (deg)	SMA[a] ($R_\odot$)	q[b]	M_{opt} ($M_\odot$)	M_X ($M_\odot$)
90	38.1	3.68	49.1	13.3
85	37.4	3.88	47.0	12.1
80	35.8	4.53	42.4	9.4
75	33.5	5.78	36.2	6.2

[a] Semimajor axis of binary system.
[b] Mass ratio (secondary over primary).

mass estimate of the compact object compared to PMM04. To do so, we correct the B and V light curves given in PMM04 for extinction and color excess. We then model these light curves using the "PHysics Of Eclipsing BinariEs" program PHOEBE (Prša & Zwitter 2005) built on top of the widely used WD program (Wilson & Devinney 1971; Wilson 1979, 1990). By adjusting the semimajor axis of the binary system, we kept the radius of the secondary star at 17 $R_\odot$. We also fixed the temperature of the secondary to 39,500 K. We then fitted the luminosity of the secondary and the mass ratio of the companions using the light curves in the B- and V-band simultaneously, assuming different inclination angles. We derive acceptable fits for inclination angles from 75° to 90°. Angles of 74° and smaller can be excluded, as the companion star would overfill its Roche lobe. The derived parameters are given in Table 3. The available optical data are not sufficient to discriminate between the allowed inclination angles. However, we expect that an inclination above 80° is more likely than an inclination in the range 75°–80°, where the companion nearly fills its Roche lobe, and unstable mass transfer would be expected based on the X-ray observations. In the case of unstable mass transfer, the X-ray emission from X-7 would most likely be much more variable on longer timescales than observed in all observations since those with the *Einstein* observatory. This implies a mass of the compact object in the system of greater than 9 $M_\odot$ and clearly indicates a black hole as the compact object in the system.

As already discussed in PMM04, further arguments for the black hole nature of the compact object in X-7 come from the lack of X-ray pulsations, the short-term variability, and the X-ray spectra. We discuss each of these properties in turn:

1. Pulsations are clear indicators of a neutron star as the compact object in a HMXB. In the power density spectrum analysis we did not detect significant periodic signals allowing a black hole as the compact object. However, this does not rule out the possibility that the compact object is a neutron star. Our unsuccessful *Chandra* periodicity search was limited toward short periods by the ACIS-I sampling time of 3.2 s. Also, with the significantly shorter sampling time of *XMM-Newton* EPIC pn of 0.073 s, PMM04 did not find significant pulsations.

2. Low accretion rate sources should show a power density spectrum (PDS) with a broken power law (see Barnard et al. 2006 and references therein). Above a luminosity of typically 0.1 of the Eddington luminosity, the PDS should be flat. The short-term fluctuations seen in the power spectral analysis of X-7 are very small, as one would expect for such a high accretion rate source. The unabsorbed luminosity of X-7 in the 0.3–10 keV band of $>1.1 \times 10^{38}$ ergs s^{-1} in maximum is consistent with a stellar mass black hole, but it does not constrain the mass.

3. HMXBs with a neutron star as the compact object normally show power-law spectra (photon index 0.8–1.5) with a high-energy cutoff around 10–20 keV (see, e.g., White et al. 1983; Makishima et al. 2000). Disk blackbody spectra, on the other hand, suggest emission that is dominated by the inner accretion disk of a low-mass XRB system, or—in the case of a HMXB—the presence of an accretion disk surrounding a black hole emitting in the high state (e.g., Makishima et al. 1986). As mentioned before, the variability of X-7 outside eclipse most likely is caused by partial covering of the X-ray emission region due to material in the accretion stream or in the outer accretion disk. If we assume that during the brightest phase, the X-7 disk blackbody normalization corresponds to the innermost stable circular orbit with radius r around a black hole, i.e., $r = 3R_S = 9 \times 10^5 (M_X/M_\odot)$ cm (with $R_S = 2GM_X/c^2$ the Schwarzschild radius), we obtain $M_X > 2.4\ M_\odot$.

All of these results of the new *Chandra* observations suggest that X-7 is the first known eclipsing HMXB with a black hole as the compact object.

Pooley & Rappaport (2005) advanced the idea of searching for eclipses in ultraluminous X-ray sources (ULXs) to determine black hole masses and, most importantly, to separate intermediate-mass black holes from stellar mass black holes as the compact object in this exceptional class of X-ray sources. They proposed to compare the number of eclipses in the different kinds of systems and predicted that more eclipses by far should be detected in stellar mass systems than in intermediate-mass black hole systems. The orbital periods and other system parameters would provide considerable insight as to the nature of the binary. While X-7 is about a factor of 5 less luminous than the commonly accepted lower limit of ULX luminosities, it is still the first eclipsing black hole XRB system and—if in other observations detected in a factor-of-5 brighter phase—may be the first stellar mass ULX candidate suitable for the proposed type of investigations.

As we discussed above, the resolved eclipse ingress and egress in the *Chandra* energy band is not caused by the extent and the structure of the X-ray-emitting region but by absorption in the density structure of the atmosphere of the companion and the accretion stream from the companion to the compact object. Watarai et al. (2005) investigated the asymmetry of black hole accretion flows and suggested the presence of effects with timescales of seconds due to relativistic effects close to the black hole. These should lead to asymmetries in the eclipsing light curves on timescales of seconds. The *Chandra* observations of the eclipse ingress and egress of X-7 show that such effects are masked by much longer timescale effects discussed above. They may only be observable by sensitive observations at higher X-ray energies such as those where absorption effects in the companion atmosphere and the accretion flow vanish.

5. CONCLUSIONS

The ChASeM33 observations clearly resolved eclipse ingress and egress of the persistent eclipsing HMXB M33 X-7. Combining the eclipse egress times with *Einstein*, *ROSAT*, and *XMM-Newton* observations allowed us to improve on the orbital period that indicates orbital decay. The X-ray spectrum can best be described by a disk blackbody spectrum with parameters that do not change significantly in different observations, while the source luminosity changes by up to a factor of 2. The short-term variability of X-7 can be described by a flat power density spectrum. No significant regular pulsations were found in the frequency range of 10^{-4} to 0.15 Hz. *HST* WFPC2 images resolve the optical counterpart, which with the help of extinction and color corrections derived from the X-ray absorption can be identified as an O6 III star.

The X-ray period and eclipse duration, together with fits to the light curve by PMM04 of the optical companion, imply a black hole with a mass above 9 $M_{\odot}$ as the most likely compact object in the system. M33 X-7 is the first eclipsing black hole HMXB.

Support for this work was provided by the National Aeronautics and Space Administration through *Chandra* award G06-7073A issued by the *Chandra X-Ray Observatory* Center, which is operated by the Smithsonian Astrophysical Observatory for and on behalf of the National Aeronautics Space Administration, under contract NAS8-03060. T. J. G. and P. P. P. acknowledge support under NASA contract NAS8-03060. This research has made use of data obtained through the High Energy Astrophysics Science Archive Research Center Online Service, provided by the NASA/Goddard Space Flight Center; of the USNOFS Image and Catalogue Archive operated by the United States Naval Observatory, Flagstaff Station (http://www.nofs.navy.mil/data/fchpix/); and of data products from the Two Micron All Sky Survey, which is a joint project of the University of Massachusetts and the Infrared Processing and Analysis Center/California Institute of Technology, funded by the National Aeronautics and Space Administration and the National Science Foundation. The authors thank Michael Bauer for his introduction to the "PHysics Of Eclipsing BinariEs" program PHOEBE. We thank the anonymous referee for his/her comments and suggestions for improving the manuscript.

Facilities: CXO(ACIS), HST(WFPC2), ROSAT(HRI), EINSTEIN(IPC)

REFERENCES

Barnard, R., Kolb, U., & Osborne, J. P. 2006, A&A, in press (astro-ph/0508284)
Blondin, J. M., Kallman, T. R., Fryxell, B. A., & Taam, R. E. 1990, ApJ, 356, 591
Blondin, J. M., Stevens, I. R., & Kallman, T. R. 1991, ApJ, 371, 684
Carroll, B. W., & Ostlie, D. A. 1996, An Introduction to Modern Astrophysics (Reading: Addison-Wesley)
Davis, J. E. 2001, ApJ, 562, 575
Dennerl, K. 1991, Ph.D. thesis, Ludwig-Maximilians-Univ. München
Dickey, J. M., & Lockman, F. J. 1990, ARA&A, 28, 215
Dubus, G., Charles, P. A., Long, K. S., Hakala, P. J., & Kuulkers, E. 1999, MNRAS, 302, 731 (DCL99)
Ebisawa, K., Day, C. S. R., Kallman, T. R., Nagase, F., Kotani, T., Kawashima, K., Kitamoto, S., & Woo, J. W. 1996, PASJ, 48, 425
Gordon, S. M., Duric, N., Kirshner, R. P., Goss, W. M., & Viallefond, F. 1999, ApJS, 120, 247
Haberl, F. 1991, A&A, 252, 272
Haberl, F., & Day, C. S. R. 1992, A&A, 263, 241
Humphreys, R. M., & Sandage, A. 1980, ApJS, 44, 319
Larson, D. T., & Schulman, E. 1997, AJ, 113, 618
Levine, A., Rappaport, S., Deeter, J. E., Boynton, P. E., & Nagase, F. 1993, ApJ, 410, 328
Levine, A. M., Rappaport, S. A., & Zojcheski, G. 2000, ApJ, 541, 194
Lewis, W., Rappaport, S., Levine, A., & Nagase, F. 1992, ApJ, 389, 665
Liu, Q. Z., van Paradijs, J., & van den Heuvel, E. P. J. 2000, A&AS, 147, 25
Long, K. S., Dodorico, S., Charles, P. A., & Dopita, M. A. 1981, ApJ, 246, L61
Makishima, K., Maejima, Y., Mitsuda, K., Bradt, H. V., Remillard, R. A., Tuohy, I. R., Hoshi, R., & Nakagawa, M. 1986, ApJ, 308, 635
Makishima, K., et al. 2000, ApJ, 535, 632
Markert, T. H., & Rallis, A. D. 1983, ApJ, 275, 571
Massey, P., Olsen, K. A. G., Hodge, P. W., Strong, S. B., Jacoby, G. H., Schlingman, W., & Smith, R. C. 2006, AJ, 131, 2478
Massey, P., et al. 2001, BAAS, 33, 1496
Nagase, F., Corbet, R. H. D., Day, C. S. R., Inoue, H., Takeshima, T., Yoshida, K., & Mihara, T. 1992, ApJ, 396, 147
Newton, K. 1980, MNRAS, 190, 689
Peres, G., Reale, F., Collura, A., & Fabbiano, G. 1989, ApJ, 336, 140 (PRC89)
Pietsch, W., Haberl, F., & Vogler, A. 2003, A&A, 402, 457
Pietsch, W., Mochejska, B. J., Misanovic, Z., Haberl, F., Ehle, M., & Trinchieri, G. 2004, A&A, 413, 879 (PMM2004)
Pooley, D., & Rappaport, S. 2005, ApJ, 634, L85
Predehl, P., & Schmitt, J. H. M. M. 1995, A&A, 293, 889
Prša, A., & Zwitter, T. 2005, ApJ, 628, 426
Safi Harb, S., Ogelman, H., & Dennerl, K. 1996, ApJ, 456, L37
Sasaki, M., Pietsch, W., Haberl, F., Gaetz, T. J., Ghavamian, P., Long, K. S., Pannuti, T. G., & Plucinsky, P. P. 2005, Astron. Tel., 633, 1
Schulman, E., Bregman, J. N., Collura, A., Reale, F., & Peres, G. 1993, ApJ, 418, L67
———. 1994, ApJ, 426, L55
Stark, A. A., Gammie, C. F., Wilson, R. W., Bally, J., Linke, R. A., Heiles, C., & Hurwitz, M. 1992, ApJS, 79, 77
van den Bergh, S. 1991, PASP, 103, 609
Watarai, K.-Y., Takahashi, R., & Fukue, J. 2005, PASJ, 57, 827
White, N. E., Swank, J. H., & Holt, S. S. 1983, ApJ, 270, 711
Wilson, R. E. 1979, ApJ, 234, 1054
———. 1990, ApJ, 356, 613
Wilson, R. E., & Devinney, E. J. 1971, ApJ, 166, 605